

# Intergranular Corrosion of Silicon-Containing Duplex Stainless Steel Weldments

D. W. Kang<sup>1,2</sup> and, H. W. Lee<sup>1,\*</sup>

<sup>1</sup> Department of Materials Science and Engineering, Dong-A University, 840 Hadan-dong, Saha-gu, Busan 49315, Republic of Korea

<sup>2</sup> Korea Institute of Nuclear Safety, Daejeon 34142, Republic of Korea

\*E-mail: [hwlee@dau.ac.kr](mailto:hwlee@dau.ac.kr)

*Received:* 12 July 2018 / *Accepted:* 1 October 2018 / *Published:* 10 April 2019

---

This study examined the effects of secondary phase and carbide formation, with varying Si content and aging time, on the intergranular corrosion of duplex stainless steel weldments. With longer aging time, accordingly greater formation of secondary phases and carbides was observed. A DL-EPR test was carried out to assess the resistance to intergranular corrosion, and from the results greater degrees of sensitization were associated with larger amounts of secondary phases and carbides. XPS depth profile results indicated the formation of SiO<sub>2</sub> at the boundary between the Cr oxide layer and the metal layer had positive effects on the intergranular corrosion resistance.

---

**Keywords:** A. Stainless steel; B. IGC; C. Passive films;

## 1. INTRODUCTION

Duplex stainless steel contains  $\delta$ -ferrite phases and austenite phases in the same proportion, and offers advantages such as outstanding resistance to corrosion and superior mechanical properties. As such, they have been widely utilized in various fields including marine structures, chemical industries, and power plants [1]. Furthermore, the increased cost of Ni in 2006 led to austenite stainless steel being replaced by duplex stainless steel, and the demand for duplex stainless steel has risen by more than 20% each year along with its expanded range of applications [2]. However, the key problem faced by industries in utilizing duplex stainless steel lies in the formation of chromium carbides, chromium nitrides, and intermetallic compounds such as  $\chi$  phases,  $\sigma$  phases, and  $\alpha'$  phases during welding between 300°C and 1000°C. These secondary phases result in chromium-depleted zones, which not only lower corrosion resistance but also toughness [3-5].

Sensitization from the formation of secondary phases during the manufacturing of stainless steel is assessed based on intergranular corrosion and other corrosion resistance tests. Strauss, Huey, and Streicher developed a method to characterize sensitization to intergranular corrosion for stainless steel [6-8], but it has disadvantages including difficult on-site implementation, inaccuracy in capturing small degrees of sensitization, and a large amount of equipment required for testing. In response to the need for quantitative measurements on the effects of precipitates and resulting degrees of sensitization, Cihal developed the Electrochemical Potentiokinetic Reactivation (EPR) test using a 2.5M  $H_2SO_4$  solution in 1969 [9]. The single loop EPR test proposed by Clarke et al. in 1977 with 0.5M  $H_2SO_4$  + 0.01M KSCN required a significant amount of time to be spent on surface finishing and grain size measurement [10]. In 1980, Akashi et al. introduced the double loop EPR (DL-EPR) test, which is not sensitive to the surface finish [11.] This DL-EPR test has been studied with a focus on austenite stainless steel, which is widely utilized in various industries, and was first applied to duplex stainless steel by Scully and Kelly in 1986 [12]. An increased demand for duplex stainless steel brought modifications to the DL-EPR test, such as using  $H_2SO_4$  with NaCl, KSCN or  $CH_3CSNH_2$  as depassivators [13-15].

Sensitization caused by secondary phases and precipitates of duplex stainless steel is not only an important factor affecting quality, but also in determining the corrosion resistance and physical properties of heat-sensitive weldments. Against this backdrop, this study seeks to examine the effects of Si content on intergranular corrosion resistance.

## 2. EXPERIMENTAL

### 2.1 Welding consumable & Welding

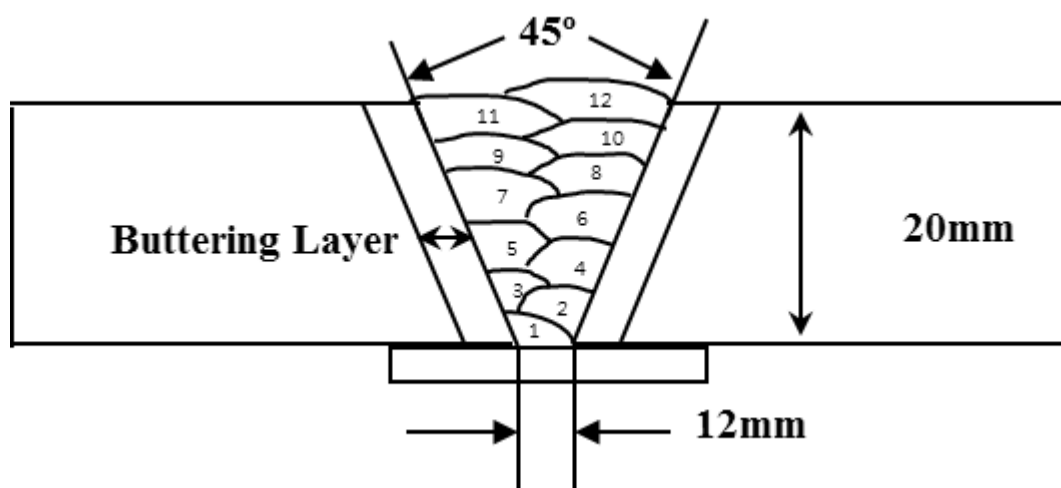


**Figure 1.** Schematic Diagrams of the weldment

The specimens were fabricated by butt welding 304 stainless steel measuring 500mm x 240mm x 20mm, with Flux-Cored Arc Welding (FCAW) as the welding method. Based on AWS A5.22 E2209T1-1 X 1.2mm, two types of wires were produced under fixed amounts of Cr, Ni, Mo, Mn, and N

and varying amounts of Si (0.9, 1.8). To minimize the influence of the parent material, buttering welding was performed once and backstrips were attached, as shown in Fig. 1. Twelve-pass welding was conducted with a root gap of 12 mm, a groove angle of 45°, 100% CO<sub>2</sub> as shielding, and a flow rate of 20 L/min. The current was DCRP, and the welding conditions are presented in Table 1.

**Table 1.** Welding Parameters.

	No	Voltage (V)	Current (A)	Travel speed (cm/min)	Heat input (KJ/cm)	Interpass temperature(°C)	pass
FCAW	0.9Si	30	200	35	10.4	MAX.150	12
	1.8Si	30	200	34	11.0	MAX.150	12
<b>Shielding gas / Flow rate : CO<sub>2</sub> 100% / 20L/min</b> <b>Polarity : DCRP / Electrode extension : 15~20mm</b>							

## 2.2 Experimental Procedure

**Table 2.** Chemical composition of the weld metal (wt%)

	<u>C</u>	<u>N</u>	<u>Si</u>	<u>Mn</u>	<u>P</u>	<u>S</u>	<u>Cr</u>	<u>Ni</u>	<u>Mo</u>
<u>0.9Si</u>	<u>0.03</u>	<u>0.14</u>	<u>0.89</u>	<u>1.02</u>	<u>0.025</u>	<u>0.004</u>	<u>22.42</u>	<u>9.5</u>	<u>3.31</u>
<u>1.8Si</u>	<u>0.05</u>	<u>0.14</u>	<u>1.76</u>	<u>0.98</u>	<u>0.025</u>	<u>0.004</u>	<u>23.16</u>	<u>9.15</u>	<u>3.07</u>

**Table 3.** Specimens Identifications

Chemical Composition	Aging Conditions	Specimen Identification	FN
0.9Si	850°C/0min	0.9Si-AS	39
1.8Si		1.8Si-AS	53
0.9Si	850°C/15min	0.9Si-15	26.3
1.8Si		1.8Si-15	36.0
0.9Si	850°C/30min	0.9Si-30	9.7
1.8Si		1.8Si-30	15.4
0.9Si	850°C/60min	0.9Si-60	3.7
1.8Si		1.8Si-60	4.5
0.9Si	850°C/120min	0.9Si-120	0.8
1.8Si		1.8Si-120	0.5
0.9Si	850°C/240min	0.9Si-240	0.3
1.8Si		1.8Si-240	0.2

The chemical composition of the deposited metals was measured using an optical emission spectrometer (Metal-Lab75/80J, GNR srl, Italy), and average values were obtained from ten measurements to reduce error, as presented in Table 2. A vacuum heating treatment furnace was employed to observe the precipitation of  $\sigma$  and  $\chi$  phases and chromium carbides from specimens having different Si content (0.9Si, 1.8Si) in relation to aging time. The specimens were aged at 850°C for 15, 30, 60, 120, and 240 minutes followed by cooling, and were denoted as shown in Table 3. The remaining amount of  $\delta$ -ferrite in each specimen was measured using a Ferrite Scope (MP30E-S, Fischer, Germany), and Table 3 shows the average values in FN from measurements by weld pass. Ten measurements were taken for the amount of  $\delta$ -ferrite, austenite, and secondary phases in the deposited metals via scanning electron microscopy with energy dispersive spectroscopy (SEM-DES) (JSM-6700f, jeol, Japan), and adjustments were made to the average values. During measurements, the acceleration voltage was 20 kV and the spot size was 3.0.

To observe the specimen microstructure using an optical microscope and scanning electron microscope, specimens were extracted from within deposited metals and subjected to electro-etching after grinding and polishing. Three types of etching solutions were used depending on the observed characteristics. To observe  $\delta$ -ferrite and austenite, 10% oxalic acid was used to perform electro-etching for 15 seconds at 3 V.  $\delta$ -ferrite and austenite were found to be significantly different in color, or specifically, grey and white. For observations of non-ideal precipitates, 10% KOH aqueous solution was used to perform electro-etching for 60 seconds at 2.5 V.  $\sigma$  and X phases were separated from other phases, to allow clearer observation. Lastly, to observe carbides and nitrates, 10% NH<sub>4</sub>OH solution was used to perform electro-etching for 40 seconds at 1.5 V.

The intergranular corrosion resistance of the specimens was assessed by the DL-EPR test in accordance with International Standard, ISO 12732-2006 [16]. The specimens were polished with 2000 grit SiC sandpaper, and the test solution was 2M H<sub>2</sub>SO<sub>4</sub> + 0.01M KSCN + 0.5M NaCl at 25±1°C. The test was conducted with an electrochemical analyzer (VersaSTAT 3 Potentiostat Galvanostat, Princeton Applied Research) with each specimen as the working electrode. The counter electrode and reference electrode were platinum foil and Ag-AgCl/KCl-sat's (0.197 Volts), respectively. The range of the potential was set to -0.3 to 0.7 V, and the scan rate was 0.2 mV/s. In the DL-EPR test, the degree of sensitization (DOS) was measured as the ratio of the maximum anode current density as the electrical potential (I<sub>a</sub>) is increased to the maximum anode current while the electric potential (I<sub>r</sub>) is decreased.

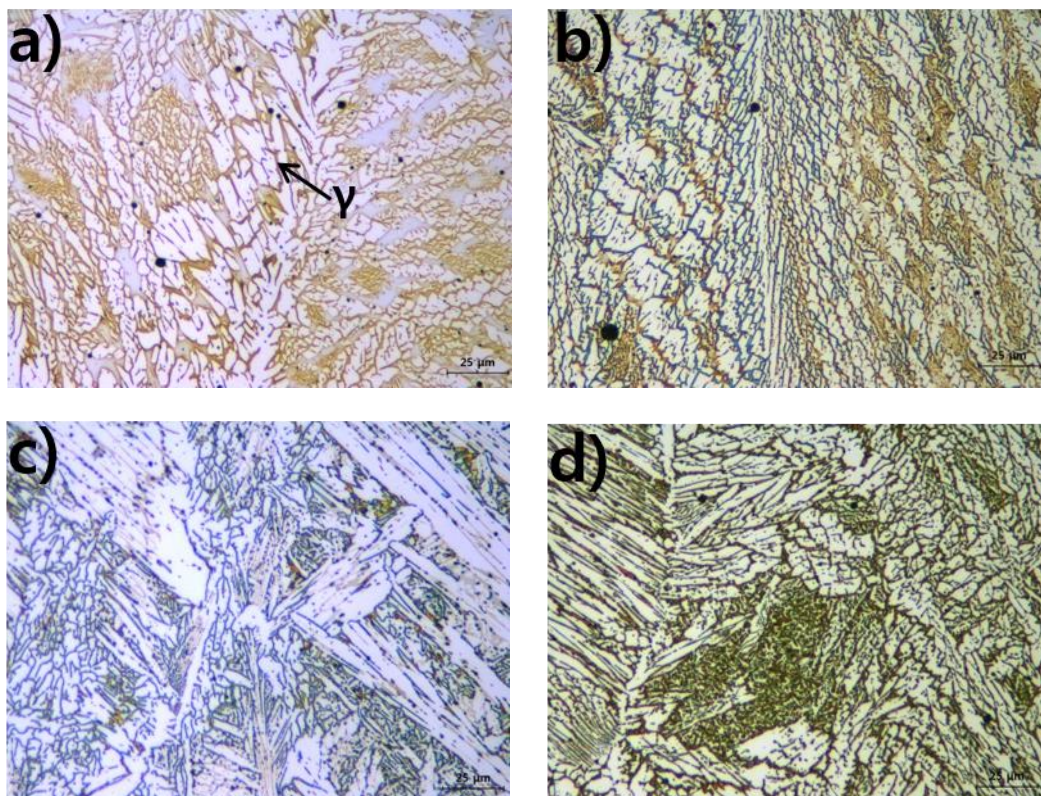
To determine the effects of Si content on the passive film, XPS depth profiling was performed with a Theta Probe Ar-XPS System (Thermo Fisher Scientific, U.K.). The X-ray source was monochromated Al K $\alpha$  (1.486.6eV) and the spot size was set as 400 $\mu$ m. All data were corrected with Cls (284.6V), and the sputtering rate was 0.1 nm/sec for SiO<sub>2</sub>.

### 3. RESULTS AND DISCUSSION

#### 3.1 Microstructural Observations and Phase Analysis

Fig. 2 shows the microstructure of each specimen observed after aging. The microstructure of duplex stainless steel in the as-weld (a), (e) state shows island-like austenite in the  $\delta$ -ferrite matrix structure [17]. However, observations made by varying the etchant only provide outlines of dark

precipitates, and do not allow  $\delta$ -ferrite and austenite to be distinguished. Comparing (b) and (f), which had the shortest aging times, black secondary phases were first precipitated from  $\delta$ -ferrite in (f). This can be explained by the higher  $\delta$ -ferrite fraction in (f), which also has higher Si content. According to past research, the addition of elements increases or decreases the proportion of  $\delta$ -ferrite and austenite, and alloying elements that affect the formation of secondary phases can be largely divided into two groups. When added as a ferrite-forming element, Si increases the proportion of  $\delta$ -ferrite by shortening the time for austenite formation due to increased  $C_{req}/N_{req}$  during cooling [18]. In (c), (d), (g) and (h), all aged for 30 minutes and 60 minutes, the growth of black secondary phases within  $\delta$ -ferrite leads to a rapid decline of  $\delta$ -ferrite and only leaves behind white austenite. Fig. 3 shows the microstructure of specimens aged for 15 minutes. Secondary austenite is observed between carbides formed at the boundary of  $\delta$ -ferrite and austenite. A study by Lee et al. showed that  $\delta \leftrightarrow M_{23}C_6 + \gamma$  occurs during aging [19].  $M_{23}C_6$  grows continuously in the direction of  $\delta$ -ferrite at the boundary between austenite and  $\delta$ -ferrite, leading to a depletion of  $\delta$ -ferrite-forming elements around carbides, and this causes  $\delta$ -ferrite to transform into austenite. The resulting austenite is called secondary austenite since it has a different composition from the existing austenite. Fig. 4 shows the microstructure after etching with  $NH_4OH$  solution, and the precipitation of carbides can be seen in relation to aging. For all specimens, chromium carbides were formed at the boundary of  $\delta$ -ferrite and austenite, and the amount of precipitated carbides increased with aging time. In addition, the amount of carbides varied with Si content. In (a) with an aging time of 15 minutes,  $\delta$ -ferrite and austenite were clearly distinct. However, they were less distinct in (b), which had less precipitation of carbides compared to (a). The same results were observed in specimens aged for 30 minutes.



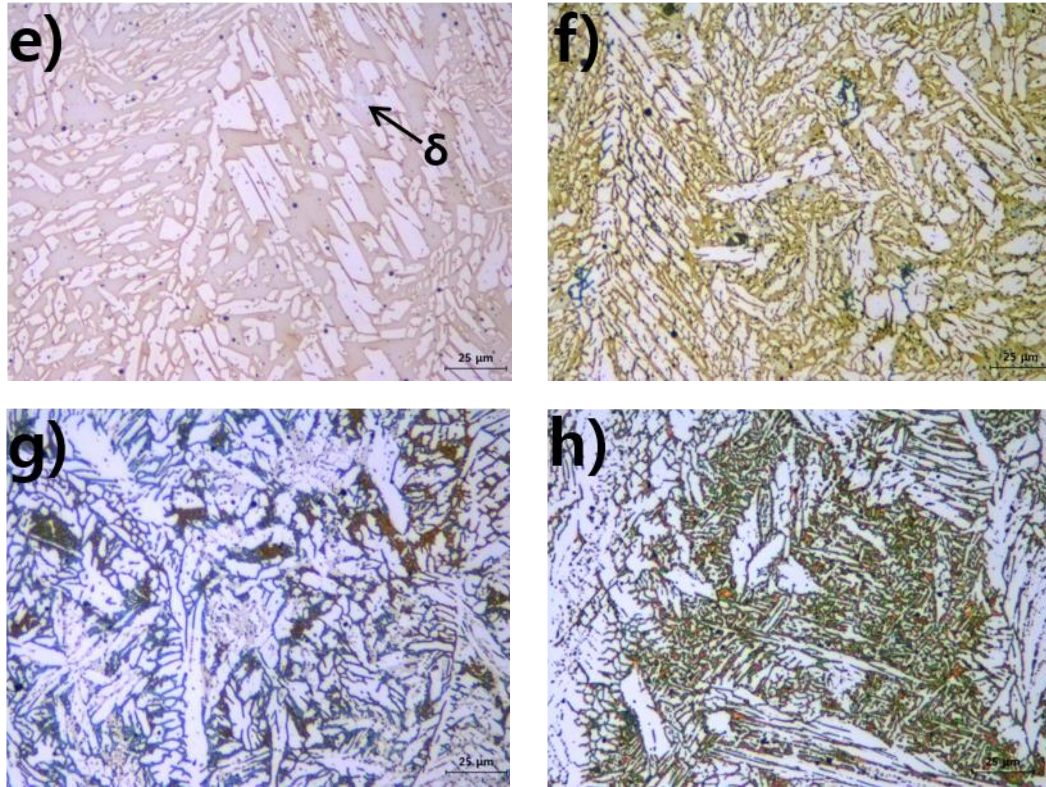


**Figure 2.** Microstructure of deposited Metal etched 10% KOH: (a) 0.9Si-as welded, (b) 0.9Si-15min aged, (c) 0.9Si-30min aged, (d) 0.9Si-60min aged, (e) 1.8Si-as welded, (f) 1.8Si-15min aged, (g) 1.8Si-30min aged, (h) 1.8Si-60min aged

Type equation here.

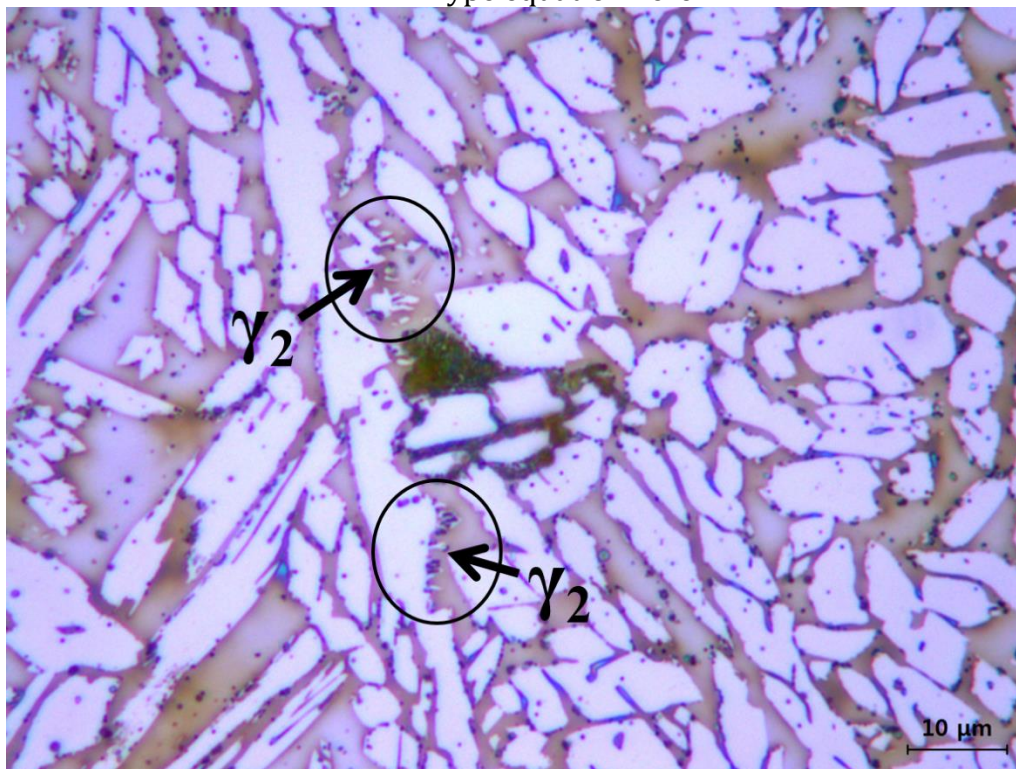


**Figure 3.** Microstructure of the lamellar precipitation after aging at 850°C for 15min

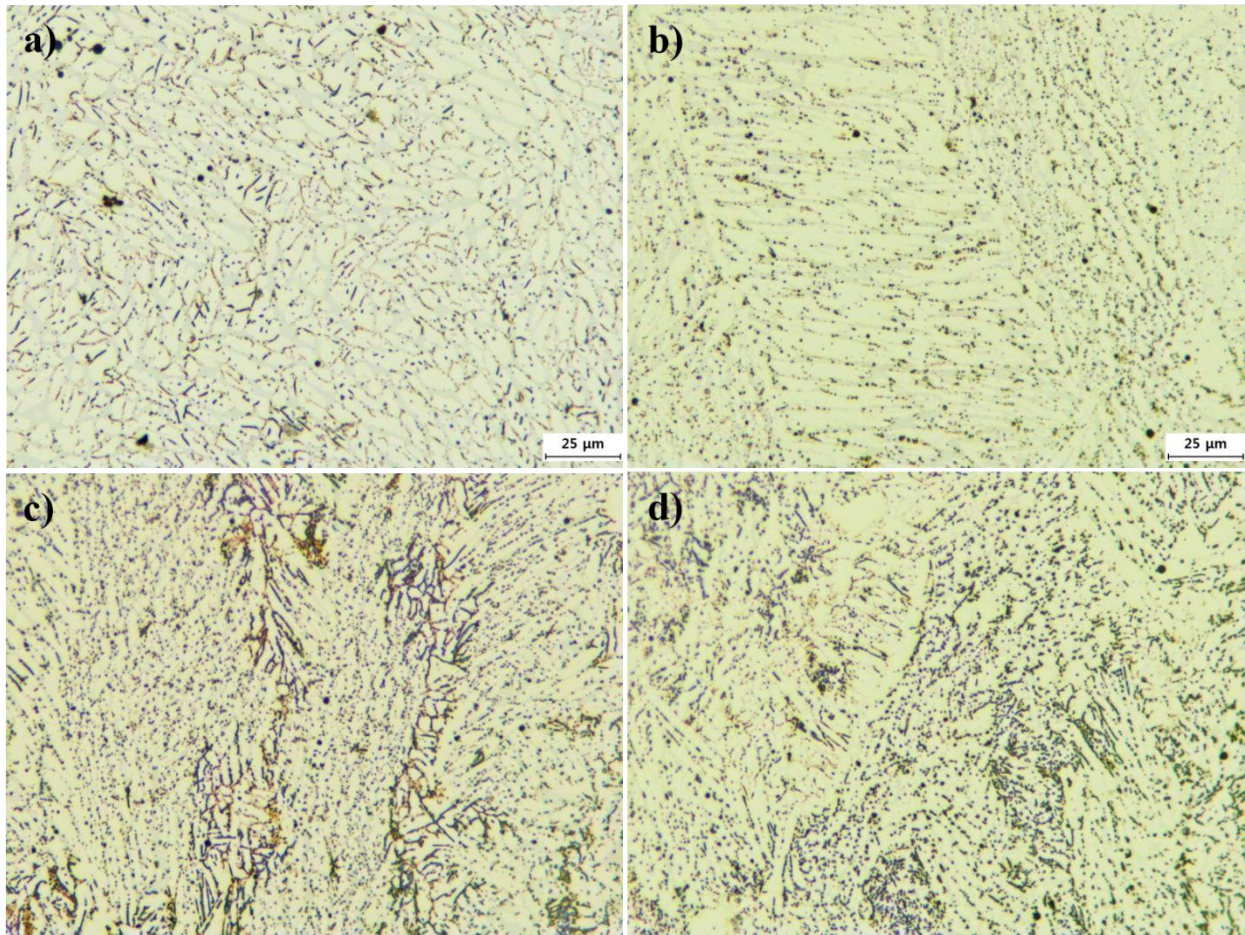
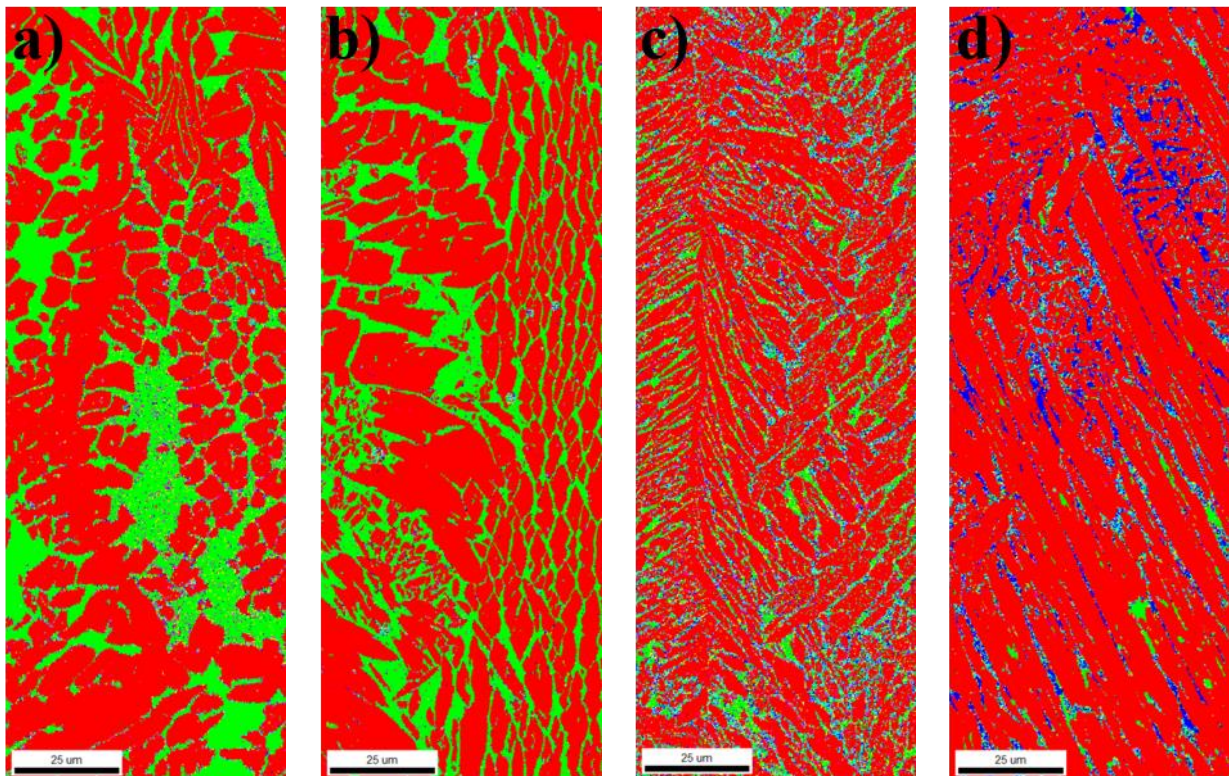


**Figure 4.** Microstructure of deposited Metal etched 10%  $\text{NH}_4\text{OH}$ : (a) 0.9Si-15min aged, (b) 1.8Si-15min aged, (c) 0.9Si-30min aged, (d) 1.8Si-30min aged

To determine the type and distribution of secondary phases and precipitates, EBSD observations were made. EBSD allows a collective organizational analysis over areas wider than that allowed by transmission electron microscopes. EBSD was applied in this study as its phase maps and grain maps are effective in observing the precipitation of secondary phases and chromium carbides [20]. Fig. 5 and Table 4 show the phase map of each specimen and the proportion of each phase in relation to aging time and Si content. Specimens (a) and (g) in the as-weld state exhibited red austenite and green  $\delta$ -ferrite, similar to the microstructure of existing duplex stainless steel, and formed small traces of carbides from thermal cycles in multi-pass welding. With an increase in aging time, both specimens (0.9Si, 1.8Si) showed a decrease in  $\delta$ -ferrite but an increase in secondary phases and carbides. The proportion of carbides decreased with increasing Si for an aging time below 30 minutes. This can be explained by the increase in C activity under higher Si content. C diffuses from areas with high Si concentration to low Si concentration [21], and the near-boundary Si causes C to move to areas of relatively lower concentration. The reduced C concentration at the boundary leads to less precipitation of carbides from carbide-forming elements such as Cr, Mo, and Mn. However, when the aging time exceeds 30 minutes, carbides are formed regardless of the Si content because of the insignificant difference in C concentration arising from long-term aging at high temperatures.

**Table 4.** EBSD phase map data : volume fraction

	Phase	As-weld	15min	30min	60min	120min	240min
<b>0.9Si</b>	$\gamma$	0.688	0.715	0.686	0.820	0.809	0.767
	$\delta$	0.250	0.253	0.114	0.034	0.030	0.039
	$\sigma$	0.003	0.009	0.029	0.076	0.072	0.091
	$\chi$	0.006	0.015	0.036	0.014	0.017	0.020
	Cr23C6	0.028	0.050	0.158	0.056	0.071	0.083
	Cr7C3	0.014	0.026	0.091	0.039	0.050	0.055
<b>1.8Si</b>	$\gamma$	0.582	0.612	0.616	0.722	0.703	0.673
	$\delta$	0.366	0.305	0.153	0.086	0.058	0.066
	$\sigma$	0.006	0.01	0.036	0.063	0.080	0.095
	$\chi$	0.017	0.024	0.037	0.027	0.032	0.029
	Cr23C6	0.01	0.018	0.044	0.034	0.040	0.040
	Cr7C3	0.01	0.011	0.091	0.068	0.087	0.095



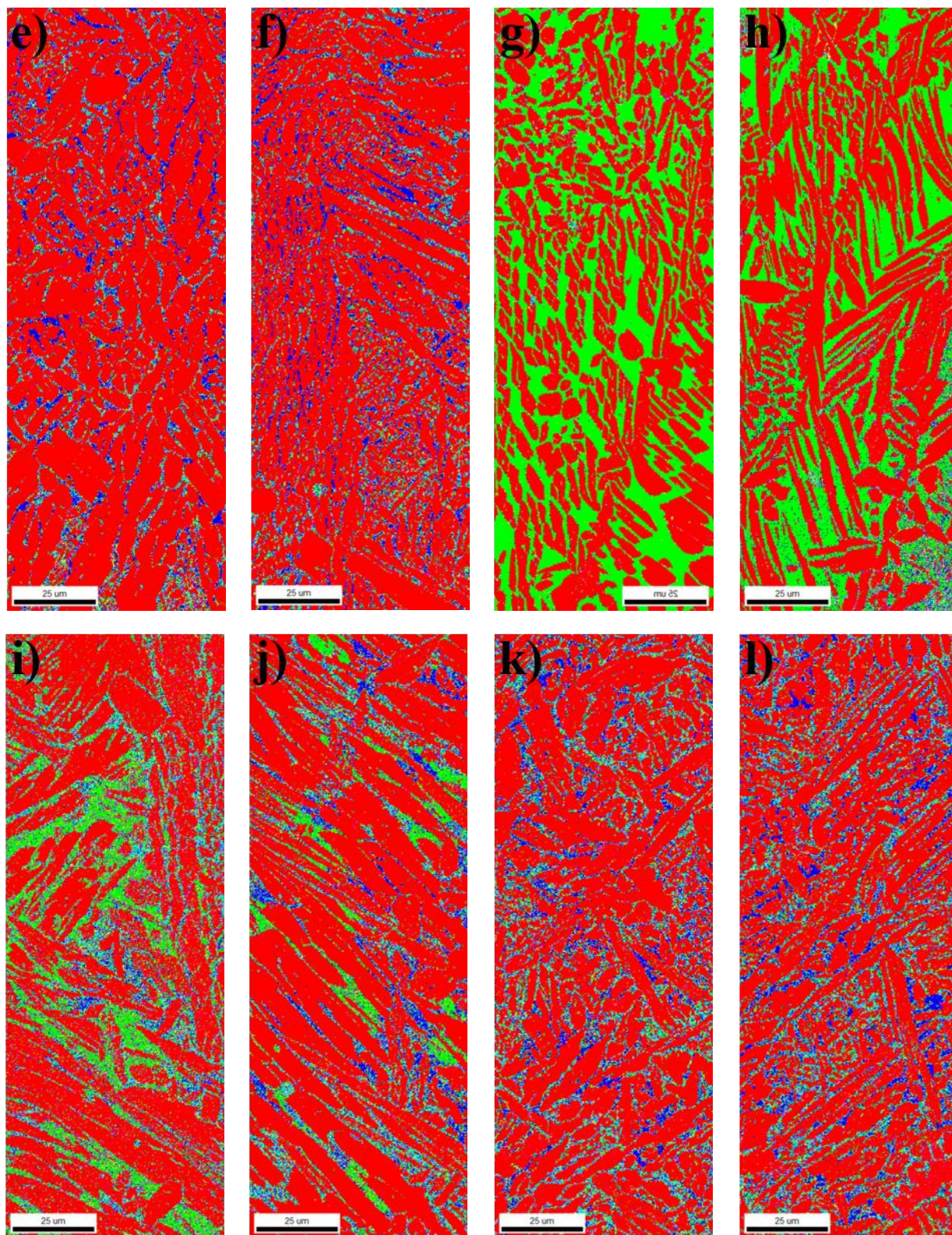


**Figure 5.** EBSD Phase map analysis of each specimens aged at 850°C in various time: a) 0.9Si-as welded, (b) 0.9Si-15min aged, (c) 0.9Si-30min aged, (d) 0.9Si-60min aged, (e) 0.9Si-120min aged, (f) 0.9Si-240min aged, (g) 1.8Si-as welded, (h) 1.8Si-15min aged, (i) 1.8Si-30min aged, (j) 1.8Si-60min aged, (k) 1.8Si-120min aged, (l) 1.8Si-240min aged

The formation of secondary phases can be largely classified according to the influence of aging time and Si content. Specimens aged for 15 minutes exhibited small traces of  $\chi$  phases, and similar to the results of Fig. 2,  $\chi$  was observed in larger amounts for the specimen with 1.8 Si. Here, the  $\chi$  phases are produced from  $\delta$ -ferrite encroaching along the boundary of austenite and  $\delta$ -ferrite, and the  $\sigma$  phase is yet to be formed. In the specimens aged for 30 minutes, there was a slight increase in  $\chi$  phases, and some were present as coarse phases due to encroachment into ferrite areas. In specimens aged for more than 60 minutes, the amount of  $\delta$ -ferrite decreased with  $\delta$ -ferrite transforming into austenite or  $\chi$  ( $\delta \rightarrow \gamma + \sigma$ ). This was accompanied by active formation and growth of chromium carbides and  $\chi$  phases. In specimens (d) and (j) aged for 60 minutes,  $\sigma$  phases were observed near or within  $\chi$  phases. Fig. 6 shows SEM images obtained to examine secondary phase precipitation. Similar to Fig. 5,  $\chi$  phases are formed at the boundary of austenite and  $\delta$ -ferrite with growth along  $\delta$ -ferrite. The  $\sigma$  phases were found to have grown from encroaching  $\chi$  phases.

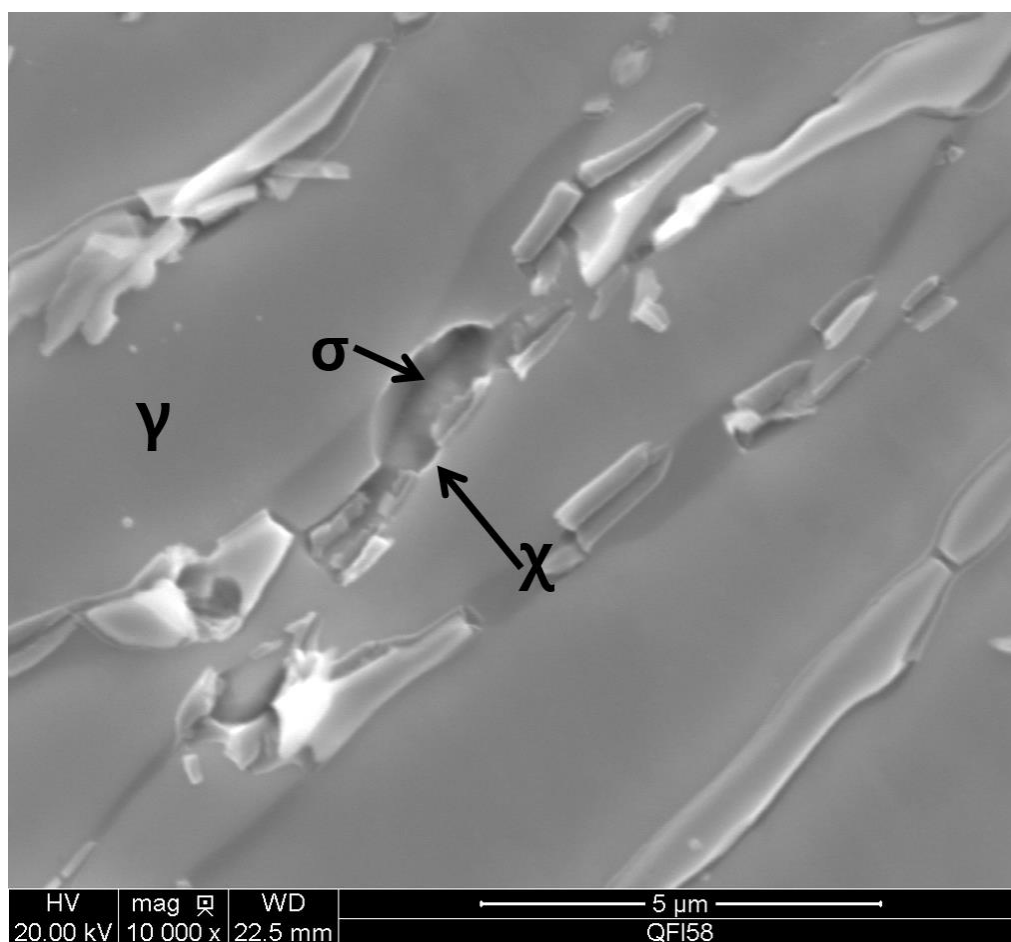


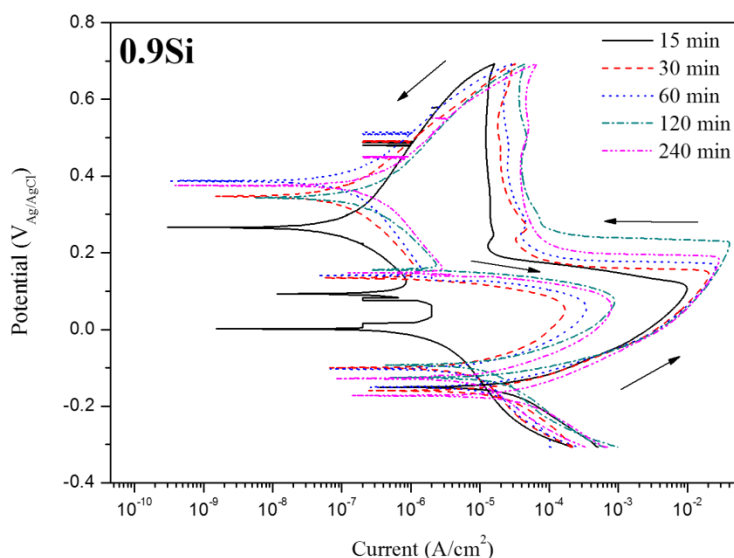
**Figure 6.** Scan Electron Micrographs(SEM) of Sigma and Chi phase in specimen aged at 850°C in 120 min

This is because the normalized thermodynamic driving force of  $\chi$  phases is larger than that of  $\sigma$  phases in the sensitization temperature range. As reported by Karlsson, the lower lattice coherency stress of  $\chi$  phases allows them to have faster nucleation than  $\sigma$  phases [22]. In other words,  $\chi$  phases with a

lower energy barrier for nucleation are precipitated first, but only stable  $\sigma$  phases remain during long-term aging in the sensitization temperature range. The  $\chi$  phases act as nucleation sites required for the formation of  $\sigma$  phases, and the resulting  $\sigma$  phases encroach on the  $\chi$  phases with aging. The two specimens with varying Si content also show different EBSD phase maps. Under the same aging conditions, the amount of secondary phases was greater for the specimen with higher Si, which is known as a ferrite-forming element. The occurrence of  $\delta \rightarrow \gamma + \sigma(\chi)$  leads to greater formation of  $\chi$  and  $\sigma$  phases with increasing Si for specimens aged for 60, 120, and 240 minutes. The greater Si content in the  $\chi$  phases compared to the austenite phases, as can be seen from the EDS results, indicates that Si accelerates the formation of  $\chi$  and  $\sigma$  phases.

### 3.2 Resistance to Intergranular Corrosion

To assess the effects of secondary phase and carbide formation on intergranular corrosion in relation to aging and Si content, a DL-EPR test was conducted using 2M  $\text{H}_2\text{SO}_4 + 0.01\text{M KSCN} + 0.5\text{M NaCl}$  at 30°C. Fig. 7 shows the results, while Table 5 gives  $I_r$ ,  $I_a$ , and DOS values. Similar DL-EPR polarization curves were observed for all specimens in Fig. 7, and passive areas ranged from +0.2 to +0.7  $\text{V}_{\text{Ag}/\text{AgCl}}$ . The critical current density  $I_a$  was observed in the big loop during increasing electric potential, but the critical current density  $I_r$  was observed in the specimens aged for 30, 60, 120, and 240 minutes as the electric potential decreased in the passive area. A difference greater than 0.1  $\text{V}_{\text{Ag}/\text{AgCl}}$  was observed between the potential at  $I_a$  and  $I_r$  for specimens with different aging times, and this is ascribed to a decrease of the ohmic resistance [23].



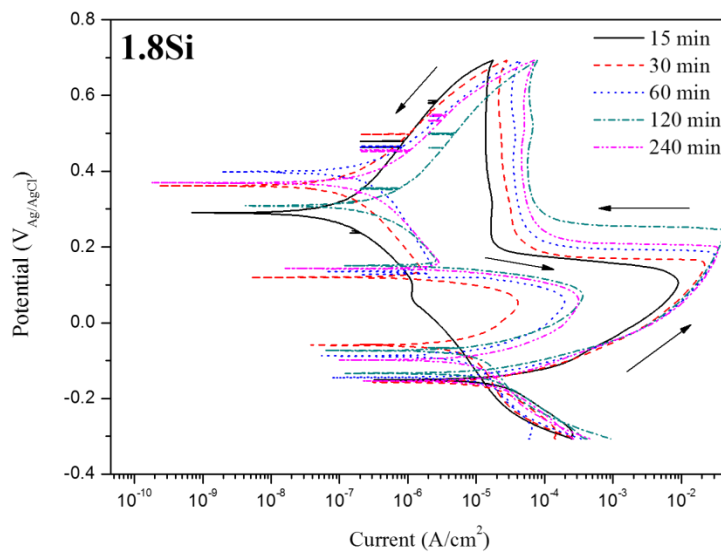


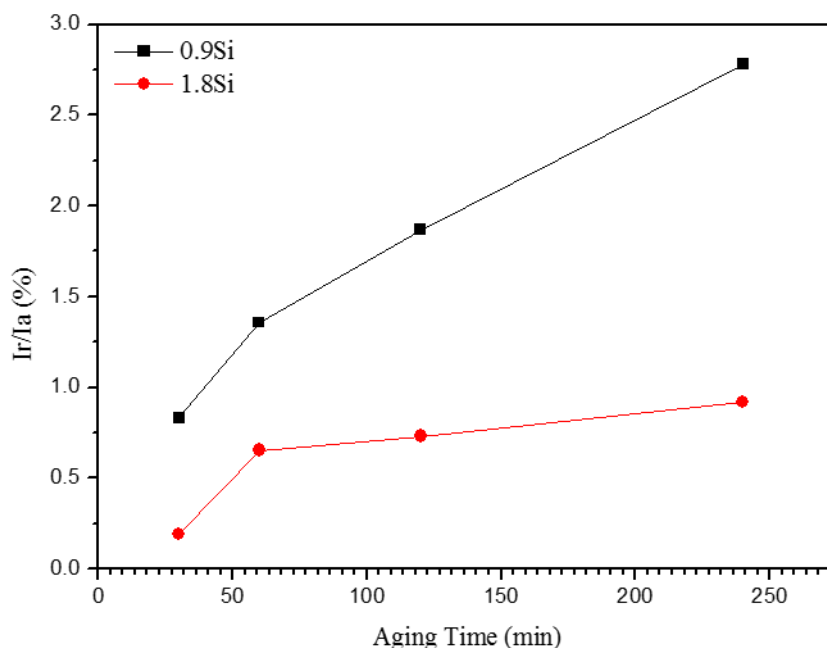
**Figure 7.** Polarization curves obtained in the DL-EPR tests on aged 0.9Si and 1.8Si DSS

In general, when assessing resistance to intergranular corrosion, the degree of sensitization ( $I_r/I_a$ ) is calculated by measuring  $I_r$  during increasing potential and  $I_r$  during decreasing potential [24]. The specimen containing 0.9 Si had  $I_a$  values of 9.8, 20.2, 25.5, 28.75, and 28.597  $A/cm^2$  with increasing aging, while the specimen containing 1.8 Si had  $I_a$  values of 8.939, 21.7, 30.2, 35.5, and 34.087  $A/cm^2$ . These results are consistent with the formation of secondary phases and carbides in Fig. 5, where greater amounts are associated with higher sensitivity to intergranular corrosion. In other words, with greater amounts of secondary phase and carbides, according more formation of Cr-depleted zones occurs. The galvanic couple formed between Cr-depleted zones and existing zones accelerates corrosion at the boundary [25]. This can also be observed through the increasing  $I_r$  value, which was measured to be 0.17, 0.35, 0.54, and 0.79  $V_{Ag/AgCl}$  with longer aging. However,  $I_r$  values were not observed for the specimen aged for 15 minutes, which had the smallest amount of secondary phases. Sensitization did not occur because Cr-depleted zones formed from carbide precipitates prevent rapid diffusion of Cr from the surrounding areas with high Cr concentration [26].

**Table 5.** Degree of Sensitization

		<b>0.9Si-15</b>	<b>0.9Si-30</b>	<b>0.9Si-60</b>	<b>0.9Si-120</b>	<b>0.9Si-240</b>
<b>0.9Si</b>	<b>I<sub>a</sub></b>	9.782	20.236	25.511	28.75	28.597
	<b>I<sub>r</sub></b>	-	0.1687	0.346087	0.538821	0.7938
	<b>I<sub>r</sub>/I<sub>a</sub>*100(%)</b>	-	0.8337	1.357	1.87	2.78
<b>1.8Si</b>	<b>I<sub>a</sub></b>	8.939	21.714	30.179	35.534	34.087
	<b>I<sub>r</sub></b>	-	0.040939	0.197089	0.259412	0.3135
	<b>I<sub>r</sub>/I<sub>a</sub>*100(%)</b>	-	0.189	0.653	0.73	0.92

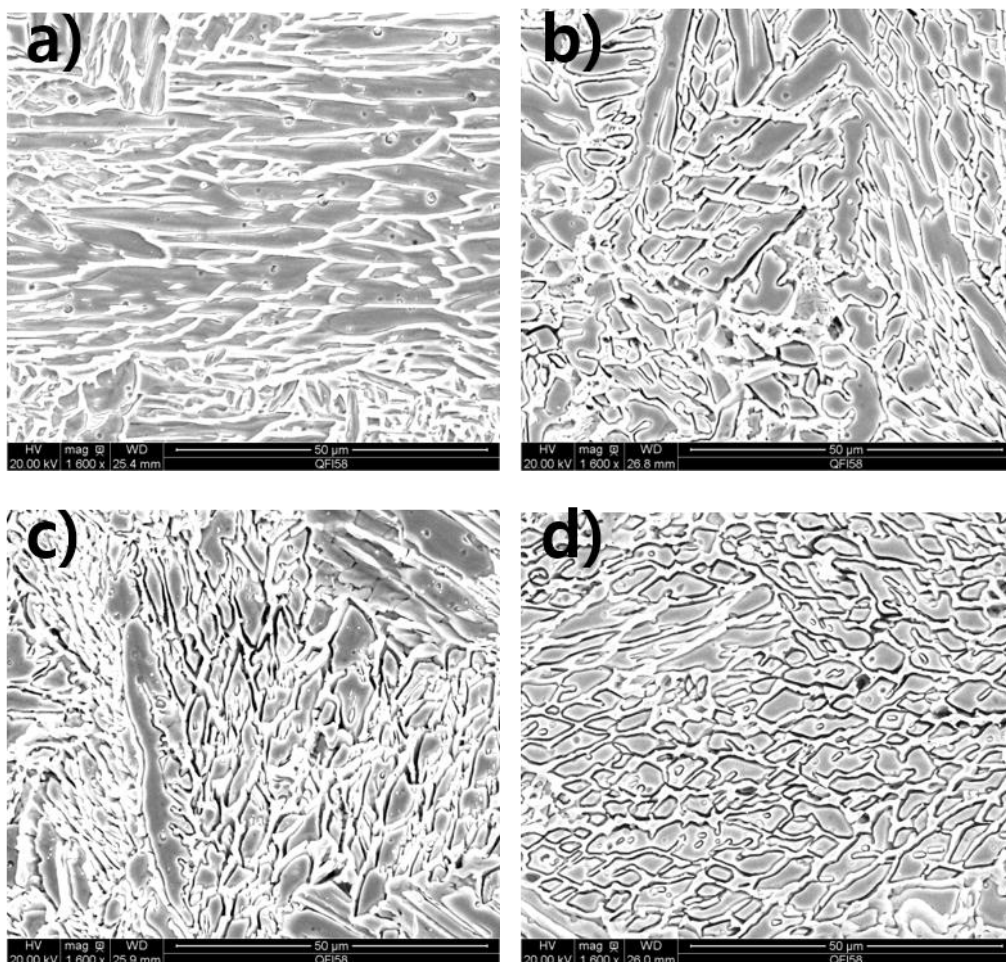
Changes in  $I_r$  and  $I_a$  values were observed in relation to Si content. The critical current density of the two specimens under the same aging conditions was higher for the specimen containing 1.8 Si since the corrosion resistance is enhanced when the addition of Si forms  $\text{SiO}_2$  and strengthens the passive film. Past research has also reported a wider passive area with the introduction of Si [27], and intergranular corrosion resistance is known to be proportionate to pitting resistance [28]. Sensitization was measured using the observed  $I_r$  and  $I_a$  values, and the results can be found in Table 5 and Fig. 8. In general, sensitization is assumed to have not occurred when the DOS value is lower than 1%, and considered high when the DOS value is greater than 5% [16]. Sensitization could not be measured for 0.9Si-15 and 1.8Si-15, which lacked  $I_r$  values. For the specimens containing 0.9 Si and 1.8 Si, the degree of sensitization rose from 0.83% and 0.19% to 2.78% and 0.92%, respectively, with longer aging at 850°C. In particular, sensitization sharply rises between 15 minutes and 30 minutes because the  $\chi$  phases and carbides encroach on  $\delta$ -ferrite and experience rapid growth, as shown in the EBSD phase map of Fig. 5. Since  $\chi$  phases are formed with diffusion of Cr and Mo from  $\delta$ -ferrite, Cr and Mo depleted zones are generated over a wide area in the surroundings, thereby causing an increase in DOS. However, the increase in sensitization is more gradual when aging is performed for 30 minutes or longer since the high-Cr and high-Mo  $\chi$  phases transform into high-Cr  $\sigma$  phases. Among the two specimens with varying Si content, the degree of sensitization was lower for the specimen containing 1.8 Si. The suppression of carbide formation leads to fewer Cr-depleted zones, and  $I_r$  and  $I_a$  values decrease as the passive film is strengthened by Si.



**Figure 8.** Degree of Sensitization values at different aging time for 0.9Si and 1.8Si

Fig. 9 shows the microstructure of specimens observed through SEM after conducting the DL-EPR test. Specimens (a) and (e), both aged for 15 minutes, did not show any intergranular corrosion. On

the other hand, specimens (b) and (f) with an aging time of 30 minutes had partial intergranular corrosion surrounding austenite, occurring locally in areas near secondary phases or precipitates. The formation of Cr-depleted zones in austenite stainless steel or duplex stainless steel usually occurs near areas with carbides having high Cr and Mo content [29,30]. As such, the formation of high-Cr, high-Mo  $\sigma$  and  $\chi$  phases results in a lack of Cr at the boundary and nearby austenite phases. The weakening of the Cr oxide layer in the Cr-depleted zones reduces the corrosion resistance, and this is represented by a high degree of sensitization. EDS was conducted with aging for 60 minutes at 850°C, and the alloying elements within austenite and  $\chi$  and  $\sigma$  phases were adjusted and are shown in Table 6. Line mapping was performed to identify Cr-depleted zones. From Table 6, we can see that the Cr content of the austenite phases remains similar. While the Cr composition of  $\chi$  phases was not significantly different from that of  $\delta$ -ferrite, the amount of Mo increased substantially. The amount of Cr was highest in the  $\sigma$  phases, which also had high Si content.



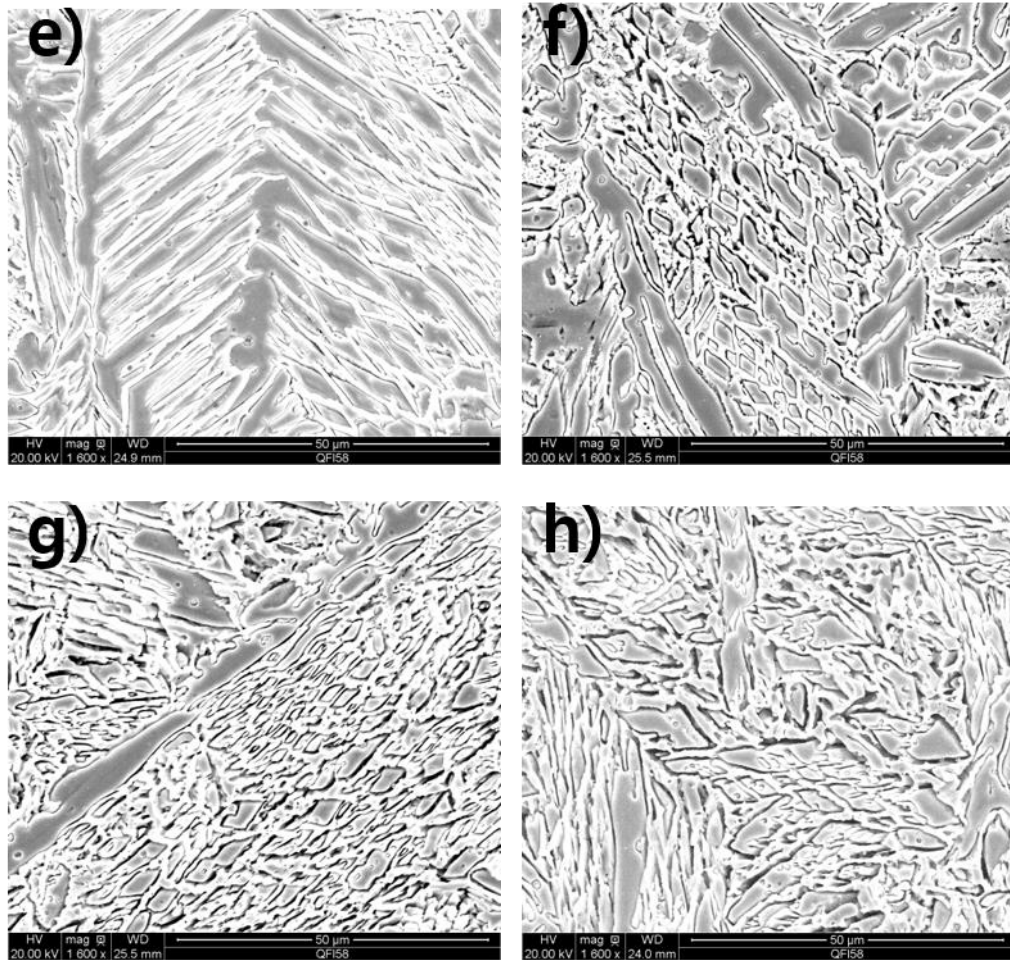


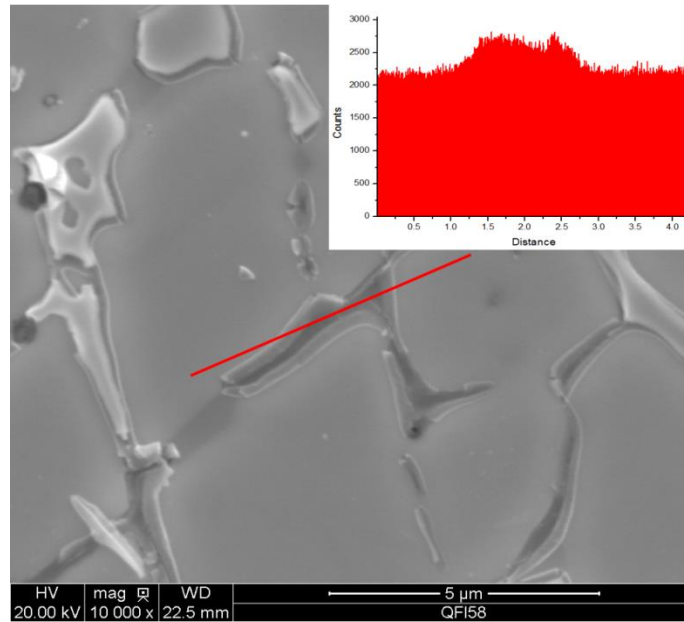
**Figure 9.** Scan Electron Micrographs(SEM) of IGC attack on specimens aged at 850°C for various time after DL-EPR test (a) 0.9Si-15min aged, (b) 0.9Si-30min aged, (c) 0.9Si-60min aged, (d) 0.9Si-120min aged, (e) 1.8Si-15min aged, (f) 1.8Si-30min aged, (g) 1.8Si-60min aged, (h) 1.8Si-120min aged

**Table 6.** SEM/EDS analysis of each phase in specimens aged at 850°C for 60min

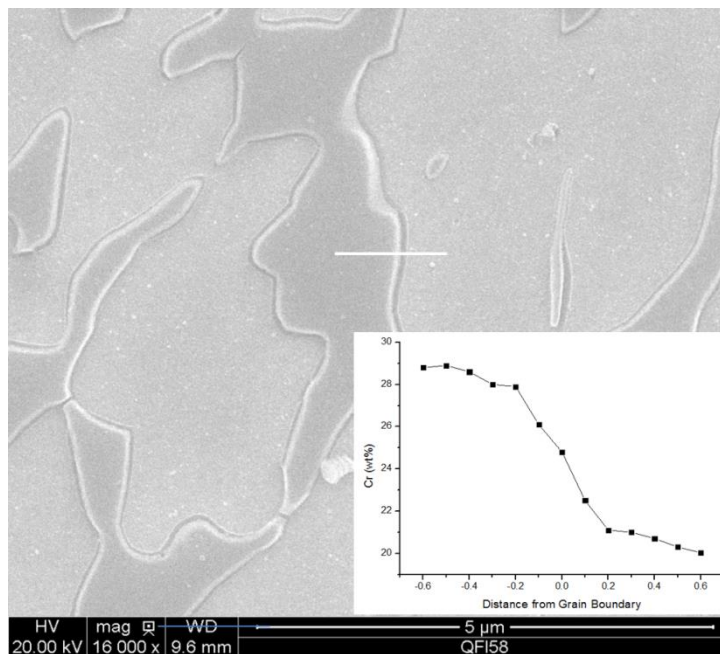
	phase	Cr	Mo	N	Si
0.9Si-60	Austenite	21.74	3.00	0.4	0.81
	X	22.84	6.28	0.48	1.09
	$\sigma$	28.79	5.62	0.19	1.17
1.8Si-60	Austenite	21.7	2.89	0.49	1.67
	X	23.11	7.53	0.43	1.95
	$\sigma$	28.92	5.38	0.46	2.03

Fig. 10 and Fig. 11 respectively shows the results of line scanning after aging for 60 and 120 minutes at 850°C. This was performed to detect chromium-depleted zones arising from the formation of chromium carbides or  $\sigma$  phases. The dark spots in the SEM images are the  $\sigma$  phases, and the bright spots are austenite. From line scanning of the boundary of austenite and  $\sigma$  phases, highlighted in red in the

figure, higher Cr content was found in the  $\sigma$  phases than in austenite. Cr depleted zones were not observed. The increase in the degree of sensitization with aging, as shown in Fig. 8, was traced to the formation of Cr-depleted zones caused by secondary phases and chromium carbides, but such zones did not show up in the line scanning results.



**Figure 10.** SEM Line Scanning in a specimens at aged 850°C for 60min and Cr profile



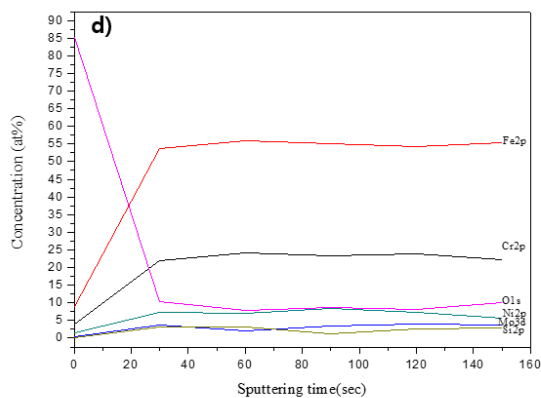
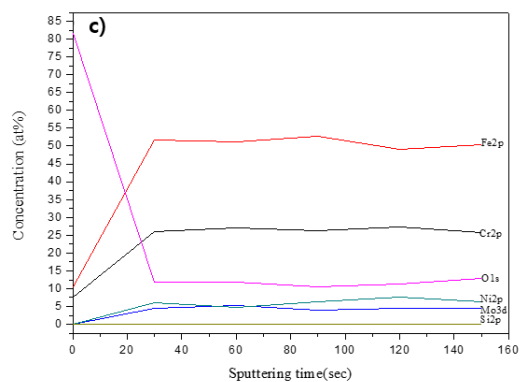
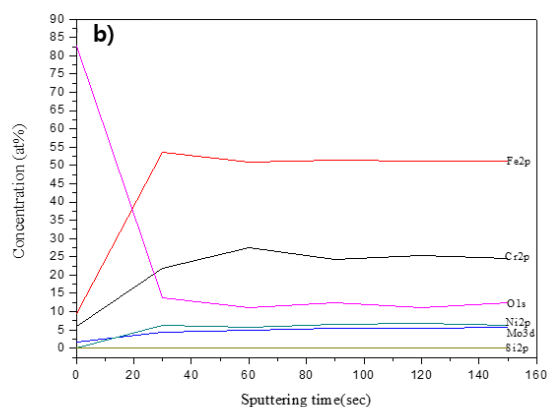
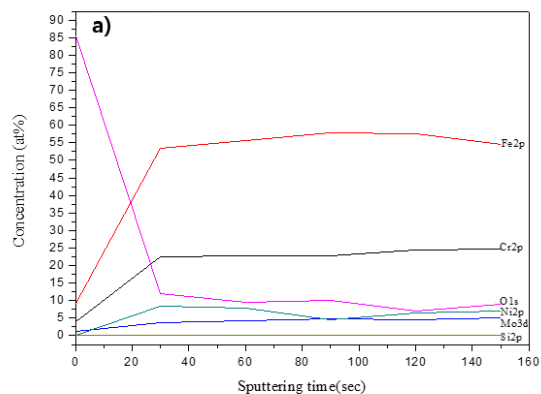
**Figure 11.** SEM/EDS analysis across the Austenite/sigma phase boundary in a sample aged at 850°C for 120min

EDS was conducted along the white line for specimens aged for 10 minutes at 850°C, but Cr-depleted zones could not be found. The failure to identify Cr-depleted zones near the boundary of austenite and  $\sigma$  phases is ascribed to the low resolution of the SEM. Cr-depleted zones are known to be formed over a very narrow area, and M.P Ryan et al. found Cr-depleted zones near MnS precipitates by using Focused Ion Beam and Secondary Ion Mass Spectroscopy (FIB/SIMIS) [31]. On the other hand, Q. Meng et al. and P. Schmuki et al. failed to find such zones despite using Scanning Auger Microscopy (SAM) and other equipment with nanometer-scale resolution [32, 33]. While this study was unsuccessful in finding chromium-depleted zones, oxide layer formation is a result of Cr depletion, and intergranular corrosion is presumed to have occurred. This coincides with the results of Table 5, which shows an increase in the degree of sensitization with aging.

### 3.3 XPS

XPS depth profiling was performed to examine the composition and depth of the passive films. For all specimens, depth profiling was carried out by measuring changes in Fe, Cr, Si, O, Ni, and Mo based on depth at one side. According to past research, a passive film of stainless steel usually consists of Cr, Cr-oxide, Fe-oxide, and small traces of Mo and Ni [34]. Among these, Cr exists as CrO(metal), CrO<sub>3</sub>, Cr<sub>2</sub>O<sub>3</sub>, and Cr(OH)<sub>3</sub>, while Fe exists as FeO(metal), FeO, Fe<sub>3</sub>O<sub>4</sub>, and FeOOH [35]. Fig. 12 shows the results of depth profiling for each specimen in relation to aging time. Vayer et al. reported that it was difficult to obtain quantitative depth measurements for stainless steel because diverse results are possible depending on the composition and depth [36]. While various methods exist to measure the passive film depth with consideration of changes in composition, this study employed the method of CM attenuation [Fe2p<sub>3/2</sub>, metal]. The attenuation of CM [Fe2p<sub>3/2</sub>, metal] method defines the point at which Fe2p no longer increases as the boundary between the passive film and metal. Regardless of aging time, the result for all specimens was 3 nm. However, with increased aging, both specimens showed a decrease in the degree of sensitization and pitting resistance but an increase in the proportion of Cr2p. This is because aging results in the formation of secondary phases and Cr carbides. With more aging, the amount of Cr2p atoms increases while that of O1s decreases, implying a decrease in the formation of Cr oxides that constitute the passive film. On the other hand, no significant changes were observed for Mo3d and Ni2p, which indicates that Mo and Ni had little effect on passive film formation.

While Si2p is not observed in any of the specimens including the specimen with 0.9 Si, Si2p atoms were found in the specimen with 1.8 Si depending on depth. An increase in Si2p atoms was detected near 3 nm, defined as the boundary of the passive film and metal in XPS depth profiling. According to Evans et al., Si is present in the form of Si oxides between the metal layer and Cr oxide layer [37]. In other words, Si strengthens the passive film through the formation of SiO<sub>2</sub> between the metal and passive film. The specimen with 1.8 Si, in which the SiO<sub>2</sub> was formed, was thus confirmed to have greater intergranular corrosion resistance and pitting resistance.



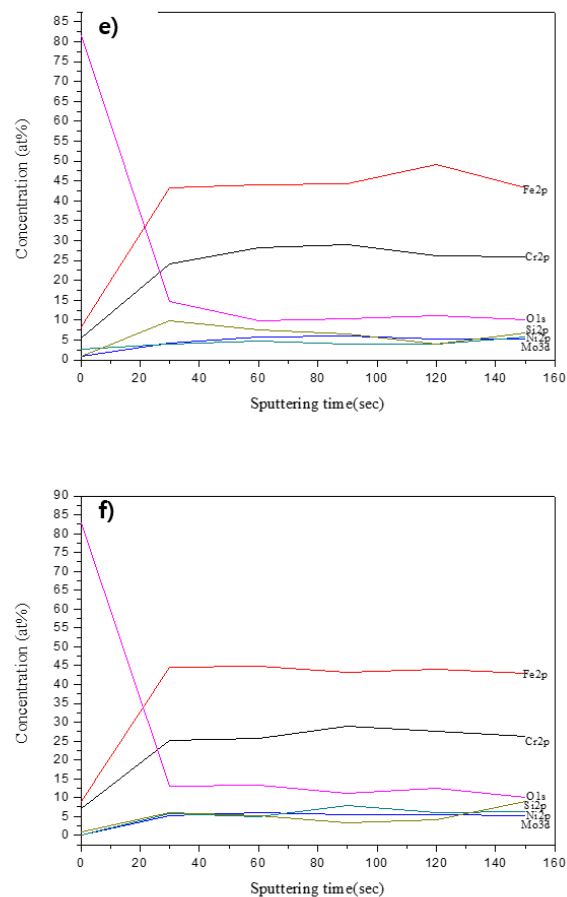


**Figure 12.** XPS depth profile of air-passivated DSS aged at 850°C in various times

#### 4. CONCLUSION

This study examined the effects of secondary phase and precipitate formation on intergranular corrosion resistance of 22Cr duplex stainless steel weldments with varying Si content and aging. The results are as follows.

1. Microstructural observations using various etchants showed an increase in the amount of secondary phases and carbides with aging at 850°C. However, under the same aging conditions, the amount of precipitated carbides decreased with greater Si because the increase in C activity suppresses carbide formation.

2. EBSD was applied to examine the precipitation of secondary phases and precipitates.  $\chi$  phases and chromium carbides were precipitated at the boundary of  $\delta$ -ferrite and austenite, and encroached into  $\delta$ -ferrite areas with longer aging time. Stable  $\sigma$  phases were formed within  $\chi$  phases during long-term aging in the sensitization temperature range, and eventually only  $\sigma$  phases remained. The proportion of secondary phases increased with Si content.

3. The DL-EPR test was performed to examine intergranular corrosion resistance. Intergranular corrosion did not occur in specimens aged for 15 minutes, but increased with aging time for specimens

aged for 30, 60, 120, and 240 minutes. Sensitization was prevented with increasing Si because the addition of Si produces SiO<sub>2</sub>, which in turn strengthens the passive film and reduces the amount of carbide precipitates.

4. SEM images obtained after the DL-EPR test showed that intergranular corrosion occurred around  $\gamma$  phases and near secondary phases and precipitates. SEM-based line scanning was performed to identify chromium-depleted zones arising from the formation of secondary phases and precipitates, but was unsuccessful due to the low resolution of the SEM.

5. XPS showed that the depth of the passive film was 3 nm regardless of aging time. Strengthening of the passive film through the formation of SiO<sub>2</sub> at the boundary between the Cr oxide layer and metal layer had a positive influence on sensitization and pitting resistance.

#### ACKNOWLEDGEMENT

This study was supported by the Dong-A university research fund.

#### References

1. S. Emami, T. Saeid, R. Azari Khosroshahi *Journal of Alloys and Compounds*, 739 (2018) 678-689.
2. James Chater : The Irresistible Rise of Duplex, *Jour. of Stainless Steel World*, KCI publishing (2017) 49-51
3. Riad Badjia,, Mabrouk Bouabdallahb, Brigitte Bacroixa, Charlie Kahlouna, Brahim Belkessac, Halim Mazac, *materials characterization*, 59 (2008) 447-453.
4. B. Deng, Y. Jiang J. Xu, T. Sun, J. Gao, L. Zhang, W. Zhang, J. Li, *Corrosion Science* 52-3 (2010) 969-977.
5. Y.H. Park, Z.H. Lee, *Materials Science and Engineering A* 297 (2001) 78-84
6. Practice A262-98, Standard Practices for Detecting Susceptibility to Intergranular Attack in Austenitic Stainless Steels, ASTM, New York (1998)
7. Test Method G28-02, Standard Test Methods for Detecting Susceptibility to Intergranular Corrosion in Wrought, Nickel-Rich, Chromium-Bearing Alloys, ASTM, New York (2008)
8. H.E. Buhler, L. Gerlach, O. Greven, W. Bleck, *Corrosion Science*, 45 (2003) 2325–2336..
9. V. Cihal, A. Desestret, M. Froment, G.H. Wagner, Étude de nouveaux tests potentiocinétiques de corrosion intergranulaire des aciers inoxydables, ÉtudeCETIM, Center de Recherches de Firminy, C.A.F.L., Rapport N 958 (1969)
10. W.L. Clarke, V.M. Romero, J.C. Danko, *Corrosion*, 77 (1977) 130–133.
11. M. Akashi, T. Kawamoto, F. Umemura, B. Gijutsu, *Corrosion Engineering*, 29 (1980) 163–169.
12. J.R. Scully, R.G. Kelly, *Corrosion*, 42 (1986) 537–542.
13. D.L. Reichert, G.E. Stoner, *Journal of The Electrochemical Society*, 137 (1990) 411–413.
14. T.F. Wu, W.T. Tsai, *Corrosion Science*, 45 (2003) 267–280.
15. S.J. Goodwin, B. Quayle, F.W. Noble, *Corrosion*, 43 (1987) 743–747.
16. International Standard, ISO 12732 Corrosion of metals and alloys – Electrochemical potentiokinetic reactivation measurement using the double loop method (based on Cihal’s method) (2006).
17. Potgietera, P.A. Olubambia, L. Cornisha, C.N. Machioa, El-Sayed M. Sherifb, *Corrosion Science*, 50 (2008) 2572-2579.
18. Iris Alvarez-Armas, Suzanne Degallaix-Moreuil “Duplex Stainless Steel”, ISTE Ltd and Wiley & Sons, Inc. (2009) 163.
19. K.M. Lee, H.S. Cho, D.C. Choi, *Journal of Alloys and Compounds* 285-30 (1999) 156-161.
20. J.H. Kang, S.H. Kim, *Journal of The Korean Metals and Materials*, 48 (2010) 730-740.
21. D. A. Porter, K. E. Easterling, Phase Transformation in Metal and Alloys, Chapman & Hall, Corn

- wall (1992)
22. H. Hoffmeister, G. Lothongkum, *Welding In The World*, 33 (1994) 2.
  23. Azar P. Majidi, Michael A. Streicher, *corrosion*, 40 (1984) 584-593.
  24. A. John Sedriks, *Corrosion Of Stainless steel*, Wiley, Inc. (1996)
  25. Denny A. Jones, *Principles and Prevention of Corrosion*, Prentice Hall, Inc (1996)
  26. David L. Reichert and Glenn E. Stoner, *Journal of The Electrochemical Society*, 137 (1990) 411-413.
  27. Robert N Gunn, *Duplex stainless steels*, Woodhead Publishing Ltd. (1997)
  28. R. Merelloa, F.J. Botanab, J. Botellaa, M.V. Matresaa, M. Marcosb, *Corrosion Science*, 45 (2003) 909-921.
  29. Hua Tan, Yiming Jiang, Bo Deng, Tao Sun, Juliang Xu, Jin Li, *Materials Characterization*, 60 (2009) 1049-1054.
  30. R.K. Dayal, N. Parvathavarthini, B. Raj, *International Material Review*, 129 (2005) 129–155.
  31. Mary P. Ryan, David E. Williams, Richard J. Chater, Bernie M. Hutton & David S. McPhail, Why stainless steel corrodes, *Nature* 415 (2002) 770-774.
  32. Q Meng, GS Frankel, HO Colijn, SH Goss, Metallurgy (communication arising): Stainless-steel corrosion and MnS inclusions, *Nature* 424 (2003) 389-390.
  33. P. Schmuki, H. Hildebrand, A. Friedrich, S. Virtanen, *Corrosion Science*, 47 (2005) 1239-1250.
  34. Aleksandra Kocijan, Crtomir Donik, Monika Jenko, *Corrosion Science*, 49 (2007) 2083-2098.
  35. Crtomir Donik, Aleksandra Kocijan, Djordje Mandrino, Irena Paulin, Monika Jenko, Boris Pihlar, *Applied Surface Science*, 255 (2009) 7056–7061.
  36. M. Vayer, I. Reynaud, R. Erre, *Journal of Materials Science*, 35 (2000) 2581-2587.
  37. H. E. Evans, D. A. Hilton, R. A. Holm, S. J. Webster, *Oxidation of Metals*, 19 (1983) 1-18.